PHYSICS

Ultra-confined mid-infrared resonant phonon polaritons in van der Waals nanostructures

Michele Tamagnone[1]*, Antonio Ambrosio[2,3,4]*†, Kundan Chaudhary[1], Luis A. Jauregui[3], Philip Kim[3], William L. Wilson[2], Federico Capasso[1]†

Hexagonal boron nitride has been proposed as an excellent candidate to achieve subwavelength infrared light manipulation owing to its polar lattice structure, enabling excitation of low-loss phonon polaritons with hyperbolic dispersion. We show that strongly subwavelength hexagonal boron nitride planar nanostructures can exhibit ultra-confined resonances and local field enhancement. We investigate strong light-matter interaction in these nanoscale structures via photo-induced force microscopy, scattering-type scanning near-field optical microscopy, and Fourier transform infrared spectroscopy, with excellent agreement with numerical simulations. We design optical nano-dipole antennas and directly image the fields when bright- or dark-mode resonances are excited. These modes are deep subwavelength, and strikingly, they can be supported by arbitrarily small structures. We believe that phonon polaritons in hexagonal boron nitride can play for infrared light a role similar to that of plasmons in noble metals at visible frequency, paving the way for a new class of efficient and highly miniaturized nanophotonic devices.

INTRODUCTION

Nanophotonics of two-dimensional (2D) and van der Waals materials is an increasingly important field due to the new physical properties of these revolutionary materials. In particular, polaritons in 2D materials, and especially plasmon polaritons in graphene, have attracted much attention as a platform for strong light-matter interaction, with applications for sensing, light modulation, and tunable antennas, to name a few (*1*–*6*). More recently, phonon polaritons in hexagonal boron nitride (h-BN) have been proposed to achieve strongly confined waveguide propagation at mid-infrared frequencies (*2*, *7*). Both the propagation of surface polaritons in h-BN flakes and the presence of standing waves in h-BN ribbons, conical frusta, and nanorods have been confirmed experimentally (*6*–*17*).

Ultra-confinement of these polaritons is possible because h-BN is a natural hyperbolic material in two wavelength regions (reststrahlen bands), namely, the RS1 band (780 to 830 cm^{-1}, where the out-of-plane h-BN permittivity ε_z is negative) and the RS2 band (1370 to 1610 cm^{-1}, where the in-plane h-BN permittivity $\varepsilon_{x,y}$ is negative), as shown in Fig. 1A. The term hyperbolic derives from the fact that the momenta k of electromagnetic waves have a hyperbolic dispersion when $\varepsilon_{x,y}$ and ε_z have opposite signs

$$\text{RS1}: \frac{k_z^2}{\varepsilon_{x,y}} - \frac{k_x^2+k_y^2}{|\varepsilon_z|} = \frac{\omega^2}{c^2} \qquad \text{RS2}: \frac{k_x^2+k_y^2}{\varepsilon_z} - \frac{k_z^2}{|\varepsilon_{x,y}|} = \frac{\omega^2}{c^2} \qquad (1)$$

This means that, in both bands, waves with arbitrarily high momenta k can exist on the hyperbola branches, resulting in high confinement, both vertically (k_z) and laterally ($\sqrt{k_x^2+k_y^2}$).

Here, we study resonating standing modes excited in subwavelength thin-patterned h-BN nanostructures. These modes can be understood

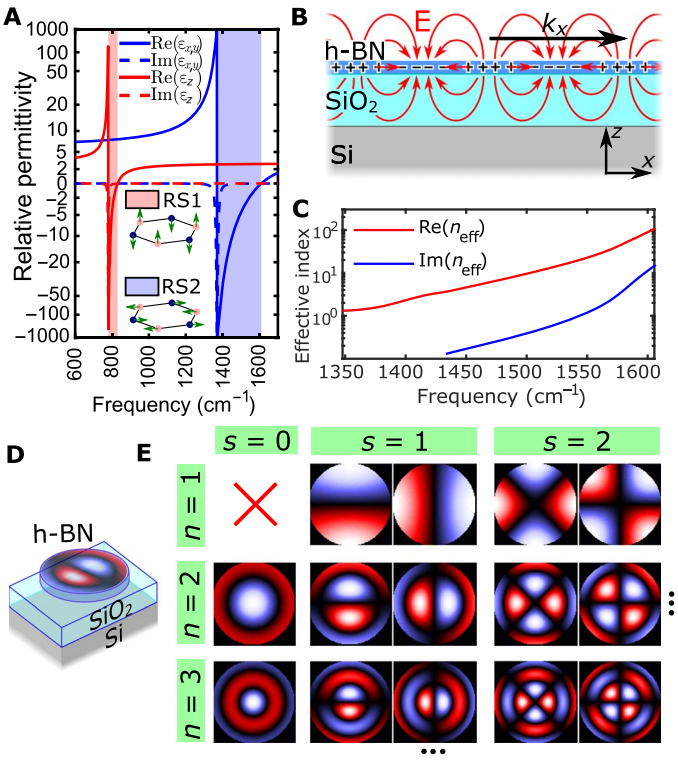

Fig. 1. Resonant modes in h-BN nanodiscs in the RS2 band. (**A**) In-plane and out-of-plane relative permittivity of h-BN; the two colored bands are the RS1 band (where $\varepsilon_z < 0$) and the RS2 band (where $\varepsilon_{x,y} < 0$). (**B**) Fundamental propagation mode supported by a 50-nm-thin h-BN on 285-nm SiO_2 on Si in the RS2 band. The electric field and the local charge density in h-BN are shown. (**C**) Numerical calculation of the mode effective index as a function of frequency. (**D**) h-BN is patterned to create particles with size 10 to 50 times smaller than the free space wavelength, which shows several resonant modes in the RS2 band that can be imaged via near-field techniques such as SNOM and PiFM. Confinement is possible owing to the hyperbolic dispersion of this material, which ensures high confinement both vertically and laterally. (**E**) Charge density for the first modes supported by an h-BN disc in the RS2 band, computed analytically from Eqs. 2 and 3. Modes are listed according to the values of the integers s and n appearing in Eq. 3. The solution for $s = 0$, $n = 1$ is the constant solution, which represents the total charge, here assumed to be 0 due to charge neutrality.

[1]Harvard John A. Paulson School of Engineering and Applied Sciences, Harvard University, Cambridge, MA 02138, USA. [2]Center for Nanoscale Systems, Harvard University, Cambridge, MA 02138, USA. [3]Department of Physics, Harvard University, Cambridge, MA 02138, USA. [4]CNR-SPIN U.O.S. Napoli, Complesso Universitario di Monte Sant'Angelo, Via Cintia, 80126 Napoli, Italy.
*These authors contributed equally to this work.
†Corresponding author. Email: ambrosio@seas.harvard.edu (A.A.); capasso@seas.harvard.edu (F.C.)

as the result of the confinement of surface waves (supported by a thin layer of h-BN) by the boundary of the structure. Multiple guided modes exist in both h-BN reststrahlen bands (*7*), but we focus here only on the fundamental propagation mode in each band, starting with the RS2 band (Fig. 1, B and C), where this mode closely resembles the geometry of plasmon polaritons in graphene (*3*, *5*).

In this case, a simple 2D wave equation can be written to describe the propagation of the surface polaritons

$$(i\omega)^2\rho = v_p^2(\omega)\nabla^2\rho \tag{2}$$

where the wave is described via the 2D charge density ρ (integrated along the thickness of the h-BN flake), and v_p is the phase velocity found from the mode dispersion relation. The standing-wave solutions can be determined by solving the wave equation using a Neumann boundary condition for the edge (derivative of ρ in the direction orthogonal to the boundary is set to 0 at the boundary). A disc with radius a (Fig. 1D) can be modeled with a circular boundary, and the modes in polar coordinates r, θ are given by (*18*)

$$\rho = J_s(k_{sn}r - \phi)(A\ \cos(s\theta) + B\ \sin(s\theta))e^{i\omega t},$$
$$k_{sn} = n\text{th root of } J_s'(ka - \phi) = 0 \tag{3}$$

where J_s is the Bessel function of order s (= 0, 1, 2, …), A and B are the arbitrary complex amplitudes, n is a nonzero positive integer, and $\phi = -0.28\pi$ is a correction term modeling the anomalous reflection phase of the edges due to the presence of evanescent fields beyond the boundary (*16*, *19*, *20*). Figure 1E lists the first modes predicted by this theory. Note that for $s = 0$, there is only one mode for each value of n, but for $s > 0$, two degenerate modes (that is, modes with the same resonant frequency) appear for each couple of n and s, which can be called the sine mode ($A = 0$) and the cosine mode ($B = 0$). Each eigen solution is represented by the resonant wave vector k_{sn}, which is linked to the resonant frequency ω_{sn} via the surface polariton dispersion equation (Fig. 1C). All the patterned

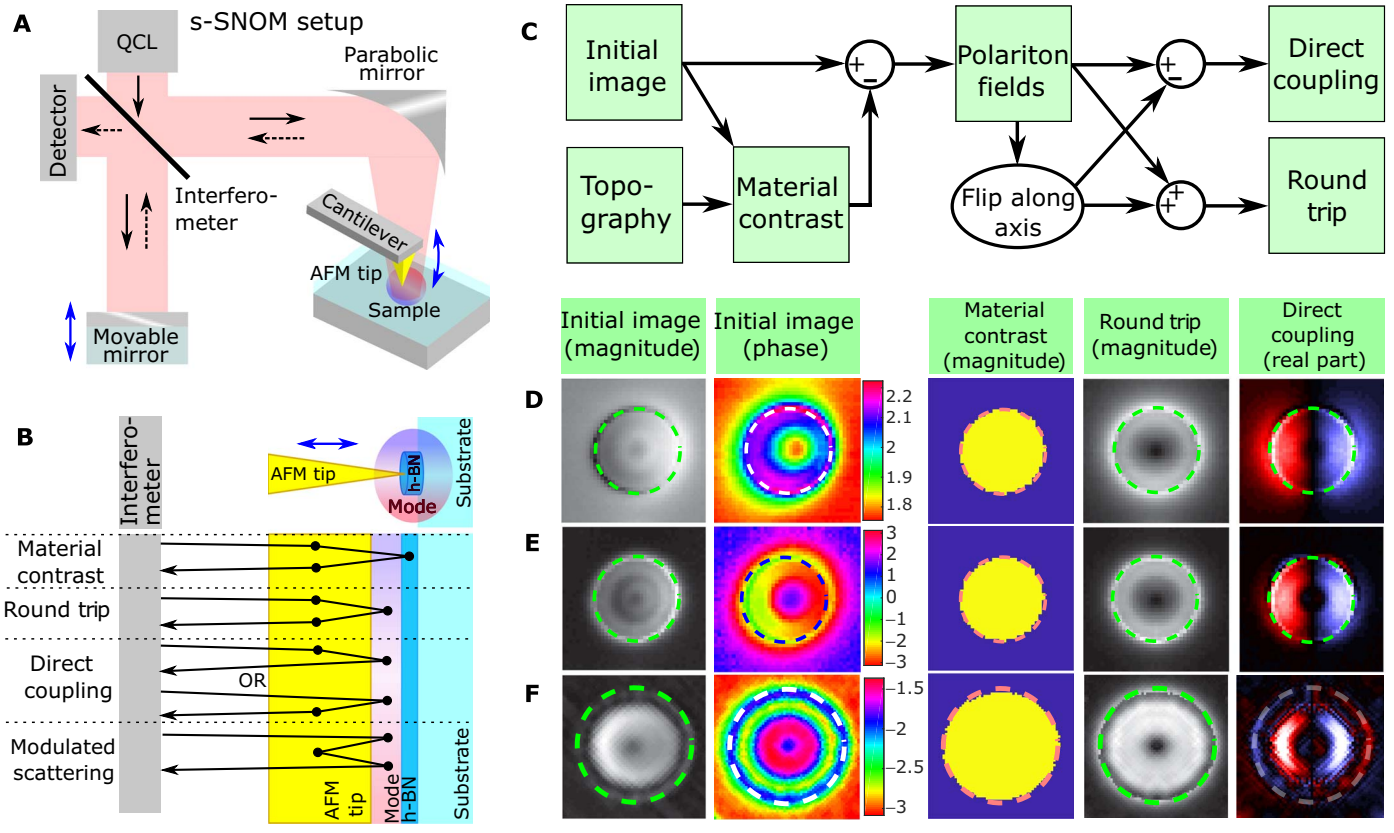

Fig. 2. Imaging resonant modes with s-SNOM. (**A**) Simplified schematic of the s-SNOM setup. The sample is illuminated by a QCL continuous-wave laser through a Michelson interferometer. An AFM tip is tapping on the sample and scatters back light, modulating it with its tapping frequency. A moving mirror, oscillating with the same frequency of the tip, is used to demodulate (pseudoheterodyne demodulation) phase and amplitude of the scattered field (that is, the complex amplitude). Images are obtained by scanning the sample (tip and laser are left in the same position). (**B**) The measured amplitude is the superposition of several contributions, listed here, each associated to a possible path of the photon in the tip-sample system. The modulated scattering contribution is very small here and can be neglected. (**C**) Procedure to separate the three contributions. First, the material contribution is measured in the center of the disc (where the E_z field of the mode is null) and on the substrate far from the disc. The two values are assigned respectively inside and outside the disc using the topography to determine the edges of the disc. Then, the material contribution is subtracted from the image. The resulting polaritonic field is the superposition of the direct and round-trip components. For bright modes, they can be separated, noting that the round-trip is even with respect to the symmetry axis of the mode, while the direct is odd. For dark modes, the direct contribution vanishes by definition. (**D**) Example of separation of contributions for the fundamental mode (1425 cm^{-1}) of a disc with diameter $D = 730$ nm, using the first pseudoheterodyne harmonic. (**E**) Same as (D) for the second harmonic. (**F**) A higher-order mode ($n = 2$, $s = 1$, 1527 cm^{-1}) using the second harmonic. Note that the direct coupling is nonzero only for bright modes (that is, only for $s = 1$).

h-BN nanostructures have been defined starting from a 50-nm-thick h-BN flake.

RESULTS

We first characterized the near field of the nanodiscs using scattering-type scanning near-field optical microscopy (s-SNOM) in the RS2 band. This technique consists of measuring the light scattered by an atomic force microscopy (AFM) tip tapping on the sample and illuminated by a coherent light source (*21*). The use of continuous-wave quantum cascade lasers (QCLs) as a source and of a pseudoheterodyne optical detection allowed us to collect both optical amplitude and phase information of the near field (Fig. 2A). The complex-valued near-field image measured with s-SNOM is the sum of several contributions, each deriving from a possible light path (Fig. 2B). The phrase "light path" indicates here the sequence of coupling steps that, starting from the incident light, leads to the scattered field detected with the pseudoheterodyne scheme. For example, incident light can couple directly with resonant optical modes (only for bright modes) or the interaction can be mediated by the AFM tip one or multiple times. The array of possible light paths, which are relevant for this experiment, is illustrated in the schematics of Fig. 2B. Only light paths interacting at least once with the AFM tip are contributing because only light modulated by the tip oscillations is detected. Here, with the word "contributions," we refer to the complex amplitude maps associated to each of these light paths.

The material contrast contribution is the one due to the local polarizability of the sample that would be observed if the sample had no boundaries, and it takes different values according to the material immediately below the AFM tip. This contribution is related to the induced dipole created by the tip on the material beneath. The round-trip contribution is due to light that is first coupled by the tip to a resonant mode, which is then coupled back by the tip to free space. For structures with circular symmetry (such as the discs), the round-trip contribution must also be circularly symmetric because it depends only on the relative position of the tip with respect to the sample. This can also be understood noting that the round-trip contribution is the sum of the squared field intensity of each mode at the used optical frequency. This implies that the sine and cosine modes are added quadratically, thus giving a circularly symmetric profile (see Supplementary Materials).

The direct coupling contribution appears instead when the incident beam excites a bright resonant mode, which then is "sampled" by the tip that scatters the local near field to the detector. Unlike the round-trip contribution, the direct coupling appears only for bright modes (that is, that can couple with the incident beam), and the image (for example, an induced dipole) depends on the direction and polarization of the incident exciting beam. Note that this contribution can also occur in the opposite way, namely, the tip injects light into a mode, which is then radiated to the detector. However, this contribution is indistinguishable from the direct one in reciprocal samples, and both are referred to as direct coupling contributions. Finally, the modulated scattering contribution occurs when the light is directly coupled in and out of the structure supporting the resonant mode, but the tip perturbs and affects the overall behavior of the resonator. This is generally negligible, unless the mode has a strongly enhanced field in a given position, as for the gap of the dipole antenna presented later. Analog contributions can be found for guided modes (*17*); in particular, self-launched guided modes (*14*) contribute to the direct coupling.

The different symmetry properties of these contributions can be used to isolate each of them in our measurements (Fig. 2C) as follows (see details in the Supplementary Materials). The material contrast is a

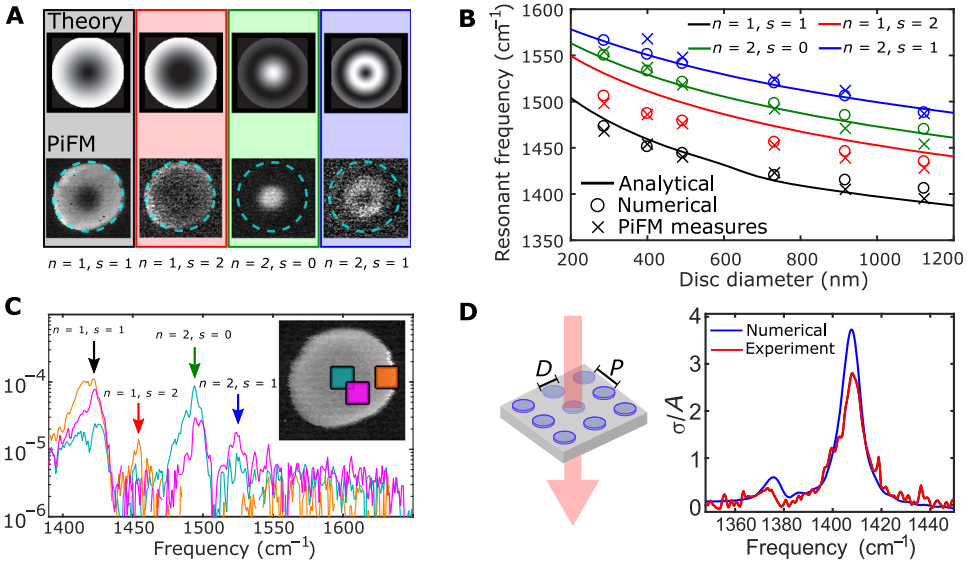

Fig. 3. PiFM imaging and extinction cross section of the nanodiscs. (**A**) Hyperspectral PiFM imaging of the first four resonance modes (for a disc of 730 nm in diameter) compared with the expected analytical mode profile. For $s = 0$, the profile is given by $|\rho|^2$ of the mode; for $s > 0$, the profile is the sum of $|\rho|^2$ of the sine and cosine modes. (**B**) Comparison of resonance frequencies of several disc modes computed analytically and numerically (using Lumerical FDTD) and measured with PiFM. (**C**) From the same hyperspectral measurement, spectra can be obtained in various points of the disc, confirming the resonant frequency of the modes in discs down to several tens of times smaller than the free space wavelength (about 7 μm). The quality factors of the resonant modes are about $Q_1 = 180$, $Q_2 = 210$, $Q_3 = 300$, and $Q_4 = 180$. (**D**) Transmission FTIR measurements of an array of h-BN nanodiscs on high-resistivity silicon (disc diameter $D = 480$ nm; periodicity $P = 1.25$ μm). The fundamental dipole mode ($s = 1$, $n = 1$) can be clearly seen, and the extinction cross section is about three times the actual area A of the disc. Quality factor is $Q_1 = 120$. The fundamental dipole mode has a resonance frequency always above the phonon resonance (1360 cm^{-1}), and this blueshift can be explained considering that the electrostatic field induced by the polarization of the disc acts as an additional restoring force, which blueshifts the overall resonance of the system.

complex value obtained from a nonresonant disc (or from the center of the disc for $s > 0$ modes, where all the remaining contributions vanish) and then subtracted from the whole disc, using the topography to identify the edges. Similarly, the material contribution of the substrate is obtained at a position far from the disc and subtracted from all points outside the disc. The remaining image is the sum of the round-trip and direct coupling contributions.

The direct coupling is extracted using the fact that it must have an odd spatial symmetry with respect to the incident wave polarization, which means that it can be extracted by subtracting from the image its flipped replica, and the remaining image is the round-trip contribution, with even symmetry. The obtained direct coupling contribution now represents the z component of the actual induced dipole field. Figure 2 (D to F) shows the resulting images for the modes ($s = 1$, $n = 1$) and ($s = 1$, $n = 2$), and the direct coupling contribution shows excellent agreement with the theory.

To effectively map the remaining modes, we used a hyperspectral photo-induced force microscopy (PiFM) setup. Unlike s-SNOM, PiFM works by mechanically detecting the gradient of the optical force generated by near fields on the AFM tip, and a pulsed laser is used as the source (*17*, *22*–*24*). The detection is fully optomechanical, and thus, no optical detector is required. The technique images the z component of the field, which has the same distribution of the local charge density due to Gauss's law. The advantage of using PiFM to characterize these structures is the possibility of acquiring hyperspectral images, thus capturing all the resonant modes in the structure with a single scan. In addition, as explained later, PiFM also allows imaging modes in the RS1 band. We observed an excellent agreement between the modes mapped with hyperspectral PiFM and the theoretically computed round-trip contribution (Fig. 3A). The resonant frequency associated to each mode agrees well with the analytical and numerical predictions for several disc sizes (Fig. 3B), and the use of the hyperspectral imaging permits the retrieval of the local spectrum in any part of the disc (Fig. 3C).

The first nontrivial mode ($s = 1$, $n = 1$) is particularly important, as it acts as a dipole mode and it can interact with an impinging plane wave (that is, it is a bright mode, which more generally holds only for modes with $s = 1$ due to symmetry-induced selection rules). Fourier transform infrared (FTIR) measurements on these discs (Fig. 3D) show that their extinction cross section equals to about three times the actual disc area at peak resonance. The resonance frequency appears blueshifted with respect to the h-BN phonon peak, which can be understood by modeling phonons in h-BN as a simple harmonic oscillator: In bulk h-BN, the RS2 phonon resonance is 1360 cm^{-1}, found from a spring-mass model, where the spring represents interatomic restoring forces and the mass is the nuclei's mass. If h-BN is patterned and the dipole mode is induced, then the Coulomb force between the charges at the two ends of the nanostructure is added to the restoring force, blueshifting the resonant frequency.

As mentioned above, for $s > 0$, two modes appear in degenerate pairs (sine and cosine). However, we can lift the degeneracy between each pair by stretching the disc in one direction to form an ellipse (Fig. 4A), and the mode with the lowest frequency will be polarized along the ellipse major axis. If two of these ellipses are placed close to each other along the major axis, separated only by a narrow gap, then the in-plane electric field shows a very strong enhancement (Fig. 4B). The structure behaves as a phonon-polaritonic antenna (*25*–*28*), similarly to plasmonic nanoantennas at visible frequencies and to graphene plasmonic antennas (*1*, *29*), with relative field enhancement up to almost 100. Numerical simulations of the Purcell factor in the antenna gap indicate values up to 80,000 for the 50-nm gap (see the Supplementary Materials for various gap sizes and a comparison with nanodiscs). This is a further demonstration of the use of these high–quality factor modes to enhance light-matter interactions, with important applications for sensing (*3*).

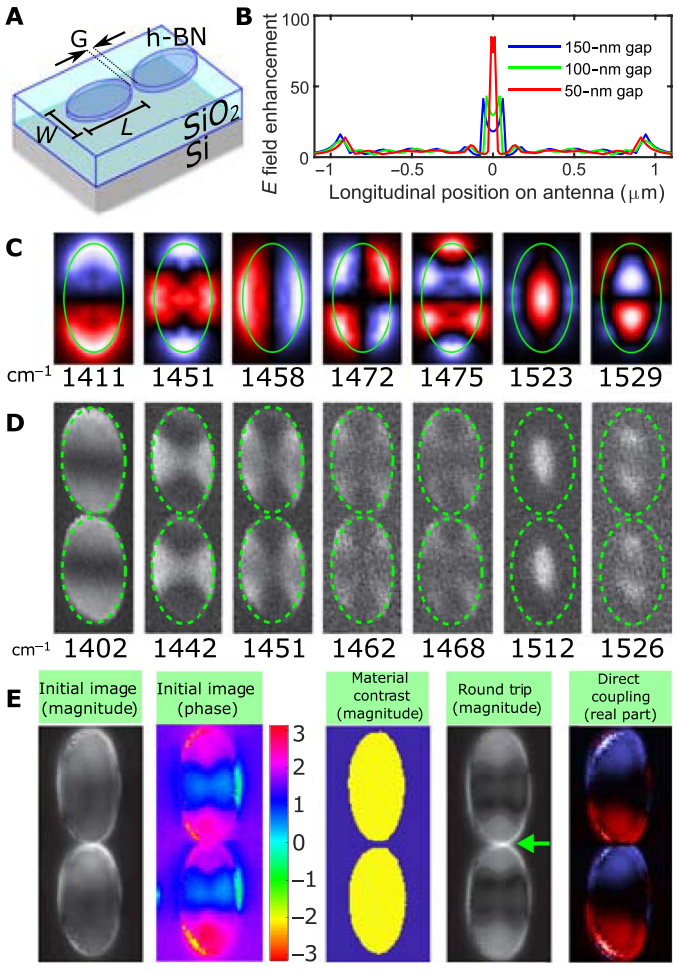

Fig. 4. Optical polaritonic dipole antennas with h-BN. (**A**) Geometry of the device (W = 440 nm, L = 850 nm, $G \cong 50$ nm, t = 50 nm). (**B**) Numerical calculation of the longitudinal field enhancement for an incident plane wave (that is, ratio of longitudinal electric field across the antenna normalized with respect to the incident field) for varying antenna gaps. Notice the strong increase of the field enhancement for small gaps, which is the behavior expected in an antenna, where the field is inversely proportional to the gap length. (**C**) Numerical simulation of the first seven resonant modes for a single elliptical antenna arm. (**D**) PiFM imaging of the first modes, which show excellent agreement with the theoretical calculations. (**E**) s-SNOM measurements (1400 cm^{-1}) with contribution separation as in Fig. 3, with incident light parallel to the dipole antenna. The fundamental mode is clearly visible both in the round-trip component and in the direct one (where the sign of the charges is visible). The green arrow indicates the modulated scattering contribution in the gap. The field in the gap cannot be seen in the direct coupling instead because it does not have a z component.

Figure 4 (C and D) shows excellent agreement between PiFM mode mapping and full-wave simulations (using Lumerical FDTD), while Fig. 4E shows the s-SNOM measurements with contribution separation as in Fig. 3, with incident light polarization parallel to the antenna. Again, the round-trip contribution is very similar to the PiFM signal, and the direct coupling matches well with the numerical mode. In the round-trip contribution, a strong signal is seen in the gap, which

can be actually attributed to the modulated scattering contribution. This occurs because the overall scattering of the dipole is strongly modulated due to the AFM tip repeatedly opening and closing the gap of the antenna, which is also a proof of the field enhancement in the gap. This effect is precisely the same exploited for modulated scattering technique for transponder antennas (*30*, *31*), which motivates the choice of the name for this contribution.

Resonances are also visible in the RS1 band in these nanoparticles (see Supplementary Materials). Because the propagating polaritons in the RS1 band have negative phase velocity, the smaller particles resonate at a lower photon frequency, and higher-order modes appear at lower frequencies. Resonances in both bands exist for arbitrarily small particle sizes, an appealing property for nanophotonics. Finally, we implemented PiFM on the same setup used for the s-SNOM, and we verified that the mode geometry is the same, taking PiFM and s-SNOM measures in the same conditions (see Supplementary Materials).

DISCUSSION

These modes are deep subwavelength, and they can be supported by arbitrarily small particles, which provide a unique way to confine light at infrared wavelengths with quality factors one order of magnitude higher than graphene plasmons or alternative technologies such as colloidal nanocrystals or quantum dots (*32*, *33*). We believe that the unique ability of phonon polaritons in h-BN nanostructures to enhance the interaction of infrared light with matter will pave the way to a new class of efficient and highly miniaturized nanophotonic devices and allows the observation of new phenomena at these wavelengths. These phonon polaritons are certainly excellent candidates to be mid-infrared counterparts for noble metal plasmons in the visible range, with important implications for future mid-infrared optical devices.

MATERIALS AND METHODS

Numerical simulations

The analytical model was solved in MATLAB, which was also used to plot the computed fields. Full-wave 3D simulations were performed with the Lumerical FDTD 3D wave solver. Field enhancement was calculated using a plane wave and by dividing the electric field amplitude on the antenna (and in the gap) by the electric field of the plane wave. Purcell factors are available in the Supplementary Materials.

Fabrication

h-BN was mechanically exfoliated onto a 285-nm SiO_2/Si substrate with predefined metallic alignment marks. The substrates were then coated with MA-N 2403 (negative electron beam resist) and exposed with an electron beam lithography system with a dose of 1200 $\mu C/cm^2$ using an accelerating voltage of 125 kV. After developing in AZ-726 for 1 min, the samples were postbaked at 100°C for 10 min. Then, h-BN was etched by using a reactive ion etching system with $CHF_3/Ar/O_2$ at flows of 10/5/2 sccm (standard cubic centimeter per minute), respectively, and a radio frequency generator at 30 W for 2 to 5 min. A further short exposure to O_2 plasma at 30 W for 30 s helped to remove any hardened MA resist. After the etching process, the exposed MA-N 2403 resist was removed by Remover PG and chloroform. Afterward, the samples were rinsed with isopropyl alcohol and dried with nitrogen. The samples on silicon were fabricated as in process above and subsequently aligned and transferred on the target Si substrate using a standard dry transfer technique.

Measurement setup

Measurement of the cross section was performed using a commercial Bruker FTIR system coupled to a HYPERION infrared microscope. s-SNOM measurements were performed with a commercial Neaspec setup. PiFM measurements were performed using a commercial Molecular Vista setup, using a pulsed QCL from Block Engineering.

Analysis of results

More details about the analysis of the results are shown in the Supplementary Materials.

SUPPLEMENTARY MATERIALS

Supplementary material for this article is available at http://advances.sciencemag.org/cgi/content/full/4/6/eaat7189/DC1

section S1. PiFM and s-SNOM schematics
section S2. Fringing field correction
section S3. Modeling of resonators fields, light path contributions, and their separation
section S4. Additional measurements
section S5. Numerical simulations of Purcell factors
fig. S1. PiFM and s-SNOM schematics.
fig. S2. Possible light paths and coupling coefficients.
fig. S3. Additional PiFM image of the dipole antenna.
fig. S4. Polaritons in discs and ellipses in the RS1 band.
fig. S5. Comparison of PiFM and s-SNOM on the same setup (Neaspec).
fig. S6. Resonance in a disc shifted from its original position.
fig. S7. Monochromatic PiFM images.
table S1. Purcell factors for nanodiscs.
table S2. Purcell factors for nanoantennas.
movie S1. Hyperspectral PiFM for different wavelengths in the RS1 band.
movie S2. Hyperspectral PiFM for different wavelengths in the RS2 band.
movie S3. Zoom-in hyperspectral PiFM for different wavelengths in the RS1 band.
movie S4. Zoom-in hyperspectral PiFM for different wavelengths in the RS2 band.

REFERENCES AND NOTES

1. M. Tamagnone, J. S. Gómez-Díaz, J. R. Mosig, J. Perruisseau-Carrier, Reconfigurable terahertz plasmonic antenna concept using a graphene stack. *Appl. Phys. Lett.* **101**, 214102 (2012).
2. D. N. Basov, M. M. Fogler, F. J. García de Abajo, Polaritons in van der Waals materials. *Science* **354**, aag1992 (2016).
3. D. Rodrigo, O. Limaj, D. Janner, D. Etezadi, F. J. García de Abajo, V. Pruneri, H. Altug, Mid-infrared plasmonic biosensing with graphene. *Science* **349**, 165–168 (2015).
4. J. Chen, M. Badioli, P. Alonso-González, S. Thongrattanasiri, F. Huth, J. Osmond, M. Spasenović, A. Centeno, A. Pesquera, P. Godignon, A. Z. Elorza, N. Camara, F. J. García de Abajo, R. Hillenbrand, F. H. L. Koppens, Optical nano-imaging of gate-tunable graphene plasmons. *Nature* **487**, 77–81 (2012).
5. A. Kumar, T. Low, K. H. Fung, P. Avouris, N. X. Fang, Tunable light–matter interaction and the role of hyperbolicity in graphene–hBN system. *Nano Lett.* **15**, 3172–3180 (2015).
6. J. D. Caldwell, A. V. Kretinin, Y. Chen, V. Giannini, M. M. Fogler, Y. Francescato, C. T. Ellis, J. G. Tischler, C. R. Woods, A. J. Giles, M. Hong, K. Watanabe, T. Taniguchi, S. A. Maier, K. S. Novoselov, Sub-diffractional volume-confined polaritons in the natural hyperbolic material hexagonal boron nitride. *Nat. Commun.* **5**, 5221 (2014).
7. S. Dai, Z. Fei, Q. Ma, A. S. Rodin, M. Wagner, A. S. McLeod, M. K. Liu, W. Gannett, W. Regan, K. Watanabe, T. Taniguchi, M. Thiemens, G. Dominguez, A. H. Castro Neto, A. Zettl, F. Keilmann, P. Jarillo-Herrero, M. M. Fogler, D. N. Basov, Tunable phonon polaritons in atomically thin van der Waals crystals of boron nitride. *Science* **343**, 1125–1129 (2014).
8. A. J. Giles, S. Dai, I. Vurgaftman, T. Hoffman, S. Liu, L. Lindsay, C. T. Ellis, N. Assefa, I. Chatzakis, T. L. Reinecke, J. G. Tischler, M. M. Fogler, J. H. Edgar, D. N. Basov, J. D. Caldwell, Ultralow-loss polaritons in isotopically pure boron nitride. *Nat. Mater.* **17**, 134–139 (2018).
9. L. V Brown, M. Davanco, Z. Sun, A. Kretinin, Y. Chen, J. R. Matson, I. Vurgaftman, N. Sharac, A. Giles, M. M. Fogler, T. Taniguchi, K. Watanabe, K. Novoselov, S. A. Maier, A. Centrone, J. D. Caldwell, Nanoscale mapping and spectroscopy of non-radiative hyperbolic modes in hexagonal boron nitride nanostructures, http://arxiv.org/abs/1710.10285 (2017).
10. F. J. Alfaro-Mozaz, P. Alonso-González, S. Vélez, I. Dolado, M. Autore, S. Mastel, F. Casanova, L. E. Hueso, P. Li, A. Yu. Nikitin, R. Hillenbrand, Nanoimaging of resonating hyperbolic polaritons in linear boron nitride antennas. *Nat. Commun.* **8**, 15624 (2017).

11. E. Yoxall, M. Schnell, A. Yu. Nikitin, O. Txoperena, A. Woessner, M. B. Lundeberg, F. Casanova, L. E. Hueso, F. H. L. Koppens, R. Hillenbrand, Direct observation of ultraslow hyperbolic polariton propagation with negative phase velocity. *Nat. Photonics* **9**, 674–678 (2015).
12. Z. Shi, H. A. Bechtel, S. Berweger, Y. Sun, B. Zeng, C. Jin, H. Chang, M. C. Martin, M. B. Raschke, F. Wang, Amplitude- and phase-resolved nanospectral imaging of phonon polaritons in hexagonal boron nitride. *ACS Photonics* **2**, 790–796 (2015).
13. A. Ambrosio, L. A. Jauregui, S. Dai, K. Chaudhary, M. Tamagnone, M. M. Fogler, D. N. Basov, F. Capasso, P. Kim, W. L. Wilson, Mechanical detection and imaging of hyperbolic phonon polaritons in hexagonal boron nitride. *ACS Nano* **11**, 8741–8746 (2017).
14. L. Gilburd, K. S. Kim, K. Ho, D. Trajanoski, A. Maiti, D. Halverson, S. de Beer, G. C. Walker, Hexagonal boron nitride self-launches hyperbolic phonon polaritons. *J. Phys. Chem. Lett.* **8**, 2158–2162 (2017).
15. X. G. Xu, L. Gilburd, Y. Bando, D. Golberg, G. C. Walker, Defects and deformation of boron nitride nanotubes studied by joint nanoscale mechanical and infrared near-field microscopy. *J. Phys. Chem. C* **120**, 1945–1951 (2016).
16. A. J. Giles, S. Dai, O. J. Glembocki, A. V. Kretinin, Z. Sun, C. T. Ellis, J. G. Tischler, T. Taniguchi, K. Watanabe, M. M. Fogler, K. S. Novoselov, D. N. Basov, J. D. Caldwell, Imaging of anomalous internal reflections of hyperbolic phonon-polaritons in hexagonal boron nitride. *Nano Lett.* **16**, 3858–3865 (2016).
17. A. Ambrosio, M. Tamagnone, K. Chaudhary, L. A. Jauregui, P. Kim, W. L. Wilson, F. Capasso, Selective excitation and imaging of ultraslow phonon polaritons in thin hexagonal boron nitride crystals, http://arxiv.org/abs/1711.04324 (2017).
18. A. B. Rabinovich, Seiches and harbor oscillations, in *Handbook of Coastal and Ocean Engineering*, Y. C. Kim, Ed. (World Scientific, 2010), pp. 193–236.
19. A. Yu. Nikitin, T. Low, L. Martin-Moreno, Anomalous reflection phase of graphene plasmons and its influence on resonators. *Phys. Rev. B* **90**, 041407(R) (2014).
20. J.-H. Kang, S. Wang, Z. Shi, W. Zhao, E. Yablonovitch, F. Wang, Goos-Hänchen shift and even–odd peak oscillations in edge-reflections of surface polaritons in atomically thin crystals. *Nano Lett.* **17**, 1768–1774 (2017).
21. N. Ocelic, A. Huber, R. Hillenbrand, Pseudoheterodyne detection for background-free near-field spectroscopy. *Appl. Phys. Lett.* **89**, 101124 (2006).
22. T. U. Tumkur, X. Yang, B. Cerjan, N. J. Halas, P. Nordlander, I. Thomann, Photoinduced force mapping of plasmonic nanostructures. *Nano Lett.* **16**, 7942–7949 (2016).
23. D. Nowak, W. Morrison, H. K. Wickramasinghe, J. Jahng, E. Potma, L. Wan, R. Ruiz, T. R. Albrecht, K. Schmidt, J. Frommer, D. P. Sanders, S. Park, Nanoscale chemical imaging by photoinduced force microscopy. *Sci. Adv.* **2**, e1501571 (2016).
24. A. Ambrosio, R. C. Devlin, F. Capasso, W. L. Wilson, Observation of nanoscale refractive index contrast via photoinduced force microscopy. *ACS Photonics* **4**, 846–851 (2017).
25. J. D. Caldwell, L. Lindsay, V. Giannini, I. Vurgaftman, T. L. Reinecke, S. A. Maier, O. J. Glembocki, Low-loss, infrared and terahertz nanophotonics using surface phonon polaritons. *Nanophotonics* **4**, 44–68 (2015).
26. R. Esteban, J. Aizpurua, G. W. Bryant, Strong coupling of single emitters interacting with phononic infrared antennae. *New J. Phys.* **16**, 013052 (2014).
27. J. D. Caldwell, O. J. Glembocki, Y. Francescato, N. Sharac, V. Giannini, F. J. Bezares, J. P. Long, J. C. Owrutsky, I. Vurgaftman, J. G. Tischler, V. D. Wheeler, N. D. Bassim, L. M. Shirey, R. Kasica, S. A. Maier, Low-loss, extreme subdiffraction photon confinement via silicon carbide localized surface phonon polariton resonators. *Nano Lett.* **13**, 3690–3697 (2013).
28. A. Huber, N. Ocelic, D. Kazantsev, R. Hillenbrand, Near-field imaging of mid-infrared surface phonon polariton propagation. *Appl. Phys. Lett.* **87**, 081103 (2005).
29. R. Filter, M. Farhat, M. Steglich, R. Alaee, C. Rockstuhl, F. Lederer, Tunable graphene antennas for selective enhancement of THz-emission. *Opt. Express* **21**, 3737–3745 (2013).
30. S. Capdevila, L. Jofre, J. Romeu, J. C. Bolomey, Multi-loaded modulated scatterer technique for sensing applications. *IEEE Trans. Instrum. Meas.* **62**, 794–805 (2013).
31. W. A. Vitale, M. Tamagnone, N. Émond, B. Le Drogoff, S. Capdevila, A. Skrivervik, M. Chaker, J. R. Mosig, A. M. Ionescu, Modulated scattering technique in the terahertz domain enabled by current actuated vanadium dioxide switches. *Sci. Rep.* **7**, 41546 (2017).
32. E. Lhuillier, S. Keuleyan, H. Liu, P. Guyot-Sionnest, Mid-IR colloidal nanocrystals. *Chem. Mater.* **25**, 1272–1282 (2013).
33. G. Konstantatos, E. H. Sargent, Solution-processed quantum dot photodetectors. *Proc. IEEE* **97**, 1666–1683 (2009).

Acknowledgments: This work was performed, in part, at the Center for Nanoscale Systems (CNS), a member of the National Nanotechnology Coordinated Infrastructure (NNCI), which is supported by the NSF under award no. 1541959. CNS is a part of Harvard University. **Funding:** This work was supported by the NSF EFRI 2-DARE program through grant no. 1542807. M.T. acknowledges the support of the Swiss National Science Foundation (grant no. 168545).
Author contributions: M.T. designed the sample and performed the numerical simulations. L.A.J., K.C., and M.T. fabricated the sample. A.A. and W.L.W. developed and performed the PiFM experimental characterization. A.A., M.T., and K.C. performed the SNOM experimental characterization. P.K. and L.A.J. provided the h-BN crystals. M.T. and A.A. developed the theory and analyzed the data. M.T., A.A., and F.C. wrote the paper with inputs from all authors. A.A., M.T., and F.C. led the project. **Competing interests:** The authors declare that they have no competing interests. **Data and materials availability:** All data needed to evaluate the conclusions in the paper are present in the paper and/or the Supplementary Materials. Additional data related to this paper may be requested from the authors.

Submitted 27 March 2018
Accepted 1 May 2018
Published 15 June 2018
10.1126/sciadv.aat7189

Citation: M. Tamagnone, A. Ambrosio, K. Chaudhary, L. A. Jauregui, P. Kim, W. L. Wilson, F. Capasso, Ultra-confined mid-infrared resonant phonon polaritons in van der Waals nanostructures. *Sci. Adv.* **4**, eaat7189 (2018).